Nonbasal Slip Systems Enable a Strong and Ductile Hexagonal-Close-Packed High-Entropy Phase

Yeqiang Bu,[1,4,*] Zhiming Li,[2,*] Jiabin Liu,[1,4,†] Hongtao Wang,[3,4,‡] Dierk Raabe,[2,§] and Wei Yang[3,4]

[1]*School of Materials Science and Engineering, Zhejiang University, Hangzhou 310027, China*
[2]*Max-Planck-Institut für Eisenforschung, Max-Planck-Straβe 1, 40237 Düsseldorf, Germany*
[3]*Institute of Applied Mechanics, Zhejiang University, Hangzhou 310027, China*
[4]*Center for X-mechanics, Zhejiang University, Hangzhou 310027, China*

Linear defects, referred to as dislocations, determine the strength, formability, and toughness of crystalline metallic alloys. The associated deformation mechanisms are well understood for traditional metallic materials consisting of one or two prevalent matrix elements such as steels or aluminum alloys. In the recently developed high-entropy alloys (HEAs) containing multiple principal elements, the relationship between dislocations and the mechanical behavior is less understood. Particularly HEAs with a hexagonal close-packed (hcp) structure can suffer from intrinsic brittleness due to their insufficient number of slip systems. Here we report on the surprisingly high formability of a novel high-entropy phase with hcp structure. Through *in situ* tensile testing and postmortem characterization by transmission electron microscopy we reveal that the hcp phase in a dual-phase HEA ($Fe_{50}Mn_{30}Co_{10}Cr_{10}$, at. %) activates three types of dislocations, i.e., $\langle a \rangle$, $\langle c \rangle$, and $\langle c + a \rangle$. Specifically, nonbasal $\langle c + a \rangle$ dislocations occupy a high line fraction of ~31% allowing for frequent double cross slip which explains the high deformability of this high-entropy phase. The hcp structure has a c/a ratio of 1.616, i.e., below the ideal value of 1.633. This modest change in the structure parameters promotes nonbasal $\langle c + a \rangle$ slip, suggesting that ductile HEAs with hcp structure can be designed by shifting the c/a ratio into regimes where nonbasal slip systems are activated. This simple alloy design principle is particularly suited for HEAs due to their characteristic massive solid solution content which readily allows tuning the c/a ratio of hcp phases into regimes promoting nonbasal slip activation.

Metals and alloys with hexagonal crystal structure are typically brittle at room temperature owing to their limited availability of internal shear carriers, referred to as dislocation slip systems. The prevalent primary basal or prismatic slip systems alone cannot accommodate plastic deformation along the c axis of the hexagonal close-packed (hcp) unit cell. Therefore, many hcp materials fail to fulfill the Taylor–von Mises criterion for homogeneous compatible deformation of a polycrystalline aggregate, rendering them brittle and texture sensitive [1,2]. Mechanical twinning or dislocation slip with a Burgers vector $\langle c + a \rangle$ on the pyramidal plane are necessary kinematic requirements for complying with general deformation states [2]. As the low symmetry of the hcp lattice puts strong geometrical constraints on twinning, nonbasal $\langle c + a \rangle$ dislocation slip is more effective in satisfying plastic compatibility. The crystallographic axial ratio of the hexagonal unit cell c/a, where a is the basal lattice axis and c is the longitudinal axis, determines activation of $\langle c + a \rangle$ slip in hcp metals [3]. Therefore, modifying the c/a ratio through alloying is an effective way to overcome the intrinsic brittleness of hcp structured alloys. Previous studies along these lines have shown that for most conventional hcp

alloys lean alloying does typically not sufficiently change the c/a ratio, e.g., for systems such as MgAl, MgZn, and MgLi (Li < 4.62 at. %) the c/a ratio is only weakly affected (See Table SI in the Supplemental Material [4]). Compared to conventional alloys with one or two prevalent base elements, the recently introduced high-entropy alloys (HEAs) with multiple principle elements [14] are much better suited for adjusting the c/a ratio by alloying due to their high solid solution content, enabling targeted compositional tuning of the c/a ratio. However, few studies were devoted so far to this aspect and the underlying deformation mechanisms of hexagonal HEAs [15–20]. To date, only several hexagonal HEAs, e.g., GdTbYDyHo [15,16], GdTbHoLaY [17], GdTbDyLuTm, and GdTbDyLuY [18], have been synthesized. Recent work [5,19–21] suggests that high-entropy hcp structures can also be obtained through phase transformation from the high-entropy face-centered cubic (fcc) matrix phase. The hcp phase in the dual-phase HEAs has been observed to play a key role in plastic accommodation and hardening at later deformation stages, which significantly contributes to the overall strength and ductility of the bulk materials [5,21,22]. Here we study the dislocation plasticity in a hcp

high-entropy phase that was recently discovered in a dual-phase HEA with a nominal composition of $Fe_{50}Mn_{30}Cr_{10}Co_{10}$ (at. %) [5,21]. We observe that, different from most conventional alloys with hcp structure, the new hcp high-entropy phase deforms not only via basal slip but also on a number of nonbasal slip carriers. This mechanism change enables compatible plastic deformation and opens a pathway to the design of novel ductile high strength HEAs with hexagonal lattice structure and compositionally adjusted c/a ratio.

The material used in this study is a four-component dual phase HEA with nominal composition $Fe_{50}Mn_{30}Cr_{10}Co_{10}$ (at. %). The detailed cast and heat treatment process has been shown in the Supplemental Material methods [4]. To prepare *in situ* TEM specimens, rectangular pieces with dimensions of $2.5 \times 5 \times 0.5$ mm^3 were machined from the recrystallized alloy sheets. The rectangular pieces were thinned by mechanical grinding down to a thickness of 60 μm. Then the pieces were further chemically thinned by twin-jet electropolishing in a solution which contained 6 vol. % perchloric acid, 34 vol. % N-butanol, and 60 vol. % methanol at $-30\,°C$. *In situ* tension was carried out in a JEM-2100 TEM operating at 200 kV at room temperature with a single-tilt tension holder (Gatan 654). Dislocations were characterized with a double-tilt holder by tilting specimens into various two-beam conditions. The dislocation core structures were characterized by scanning transmission electron microscopy (STEM) in a JEM-ARM200

electron microscope. XRD was carried on different areas of fractured samples after tensile and analyzed by Rietveld analysis in conjunction with the TOPAS software package to retrieve lattice parameters.

Figure 1 shows the microstructure of a deformed region containing the hcp phase subjected to *in situ* tension. The hcp phase is outlined by yellow dashed lines in Fig. 1(a). Figure 1(b) shows the dark-field TEM image which highlights the morphology of the hcp phase. The inset in Fig. 1(b) shows the electron diffraction pattern taken from the hcp region with a zone axis of $[1\bar{2}13]$. The deformation modes active in the hcp phase under *in situ* tension loading were dynamically captured in TEM as shown in the movie in the Supplemental Material [23]. From the *in situ* imaging, we observe that the deformation of this hcp high-entropy phase is dominated by dislocation slip. Figures 1(c)) and 1(d) are two key snapshots from the movie in the Supplemental Material [23]. As the inset in Fig. 1(c) reveals, this *in situ* movie was captured under two-beam condition with an operating vector of $\boldsymbol{g} = [10\bar{1}1]$ close to $\boldsymbol{B}/\!/[1\bar{2}13]$. Five dislocations are labeled as $D1 - D5$ in Fig. 1(c). After 32 sec, the $D1$ dislocation glides out of the field of view and a new dislocation ($D6$) emerges following the dislocation array shown in Fig. 1(d). The slip traces left by the dislocation slip are outlined in Fig. 1(c), and those slip traces are determined to be parallel to the $(01\bar{1}1)$ plane. According to the slip traces, we speculate that the dislocations marked by red arrows are slipping on the $(01\bar{1}1)$ planes. In the hcp crystal structure, $(01\bar{1}1)$ planes are pyramidal planes. This suggests that nonbasal slip can indeed occur in this hcp high-entropy phase.

Following the *in situ* tensile experiments, detailed TEM analysis was performed using a double-tilt holder to investigate the full character of the dislocations active in the hcp phase by using various imaging vectors. Figure 2 displays TEM images of different types of dislocations in the hcp high-entropy phase. They were obtained under different two-beam conditions. The dislocation types in all images were determined according to the $\boldsymbol{g} \cdot \boldsymbol{b}$ extinction criterion (See Table SII in Supplemental Material [4]). Figures 2(a)–2(c) were taken under $g = [0002]$, $g = [01\bar{1}0]$ and $g = [01\bar{1}1]$ two-beam conditions around the $[2\bar{1}\,\bar{1}\,0]$ zone axis, respectively. Figure 2(d) was taken under the $g = [2\bar{1}\,\bar{1}\,0]$ two-beam condition around the $[01\bar{1}0]$ zone axis. Figure 2(e) is a schematic diagram showing the observed dislocations labeled by A to J. The strong contrast of dislocations A to H under the $g = [0002]$ two-beam condition suggests that they are $\langle c \rangle$ or $\langle c + a \rangle$ dislocations. Furthermore, the dislocations A to F are always visible under $g = [01\bar{1}0]$, $g = [01\bar{1}1]$, and $g = [2\bar{1}\,\bar{1}\,0]$ two-beam conditions, suggesting that they are $\langle c + a \rangle$ dislocations ($b = 1/3\langle 2\bar{1}\,\bar{1}\,3\rangle$). Dislocations G and H are invisible under the $g = [2\bar{1}\,\bar{1}\,0]$ two-beam conditions, meaning that they are $\langle c \rangle$ dislocations ($\boldsymbol{b} = \langle 0001 \rangle$). Dislocations I and J are invisible under the $\boldsymbol{g} = [0002]$ two-beam condition and
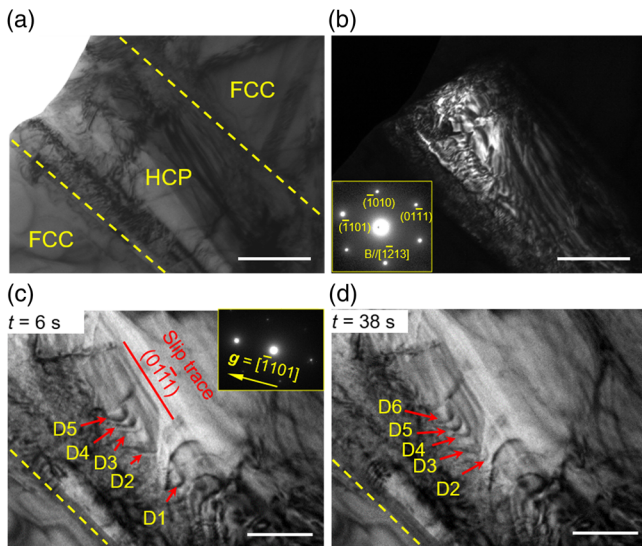

FIG. 1. Nonbasal slip in the hcp high-entropy phase. (a) Bright-field TEM image of a region containing hcp phase. (b) Dark-field TEM image showing the morphology of the hcp phase. The inset gives the electron diffraction pattern of the hcp phase taken under $B/\!/[1\bar{2}13]$. (c) and (d) Two sequential images from the *in situ* movie. The yellow dashed lines represent the interfaces between the hcc and hcp phases. The scale bars in (a) and (b) are 500 nm, in (c) and (d) are 200 nm. Full details of the dislocation dynamics are given in movie in the Supplemental Material [23].
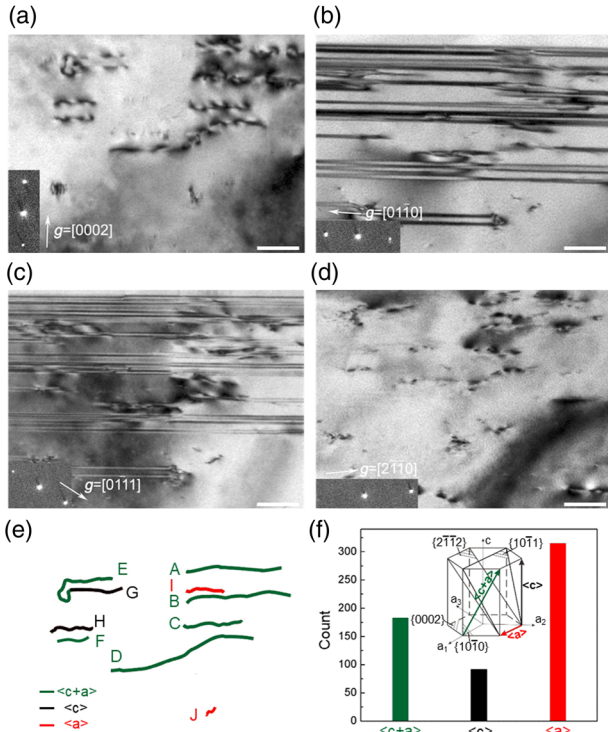
FIG. 2. Morphology of dislocations in the hcp high-entropy phase under various two-beam conditions. (a) $g = [0002]$, (b) $g = [01\bar{1}0]$, (c) $g = [01\bar{1}1]$, and (d) $g = [2\bar{1}\,\bar{1}0]$. (e) Schematic illustration of the different types of dislocations. (f) Statistical results of the three types of dislocations in the hcp high-entropy phase after *in situ* tensile deformation. The inset displays the Burgers vector direction of each dislocation type and some important slip planes. Scale bars in (a)–(d) are 70 nm.

FIG. 3. Atomic-resolution images of (a) an $\langle a \rangle$ dislocation and (b) a $1/2\langle c + a \rangle$ dislocation core structure in the hcp high-entropy phase. Scale bars in (a) and (b) are 1 nm.

are visible under other two-beam conditions, suggesting that they are $\langle a \rangle$ dislocations $(b = 1/2\langle 2\bar{1}\,\bar{1}0 \rangle)$. The frequency of the three types of dislocations was statistically analyzed by investigating a number of hcp grains (27) under various two-beam conditions. More TEM images of the analyzed hcp grains and dislocations are shown in Table SIII and Figs. S1–S6 in the Supplemental Material [4]. The line fractions of $\langle c + a \rangle$, $\langle c \rangle$, and $\langle a \rangle$ dislocations were calculated to be 31%, 16%, and 53%, respectively, as summarized in Fig. 2(f). This means that about half of the dislocations have nonbasal character.

Figures 3(a) and 3(b) display the inverse fast Fourier transformed images correspond to atomic-resolution high angle annular dark-field (HAADF)-STEM images of the core structures of $\langle a \rangle$ and $1/2\langle c + a \rangle$ $(b = 1/6\langle 20\bar{2}3 \rangle)$ dislocations in the hcp high-entropy phase, respectively. $1/2\langle c + a \rangle$ dislocations could be produced by the dissociation of $\langle c \rangle$ or $\langle c + a \rangle$ dislocation [24]. The dissociation is due to the large Burgers vectors and high energy of the $\langle c \rangle$ and $\langle c + a \rangle$ dislocations. This dissociation is beneficial for the actuation of $\langle c + a \rangle$ slip and thus providing better deformation compatibility among the differently oriented crystals. The Burgers vectors have been examined through
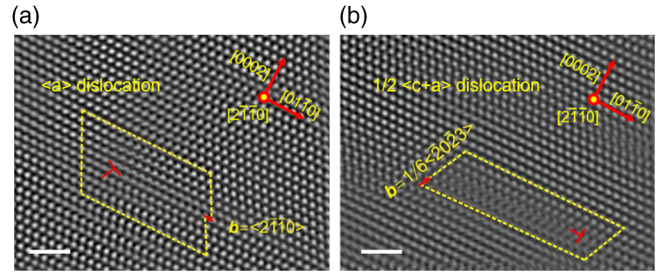
Burgers circuit analysis in the atomic-resolution images. The atomic-resolution images further confirm the activities of $\langle a \rangle$, $\langle c \rangle$, and $\langle c + a \rangle$ dislocations in the hcp high-entropy phase. The raw HAADF-STEM data of the dislocation core structures are shown in Fig. S7 in the Supplemental Material [4].

Some step-shaped dislocations were found in the hcp high-entropy phase, e.g., the dislocation D, which is a $\langle c+a \rangle$ dislocation as shown in Fig. 2(e) (more step-shaped dislocations are shown in Fig. S8 in the Supplemental Material [4]). The step-shaped configuration reveals double cross slip of the $\langle c + a \rangle$ dislocation. Figure 4 provides further characterization of the $\langle c + a \rangle$ dislocation D at higher magnification under $g = [0002]$ two-beam conditions around the $[2\bar{1}\,\bar{1}0]$ zone axis. Two straight segments of the dislocation are parallel to the $[01\bar{1}0]$ direction, and the angle between the inclined segment and the straight segment is 30° [Fig. 4)]. Geng *et al.* [25] and Jain *et al.* [26] observed similar step-shaped configurations of the $\langle c + a \rangle$ dislocations in Mg alloys. They proposed that such step-shaped dislocation configurations, observed postmortem, i.e., after unloading, were residuals of the preceding cross-slip process of the $\langle c + a \rangle$ dislocations. According to the
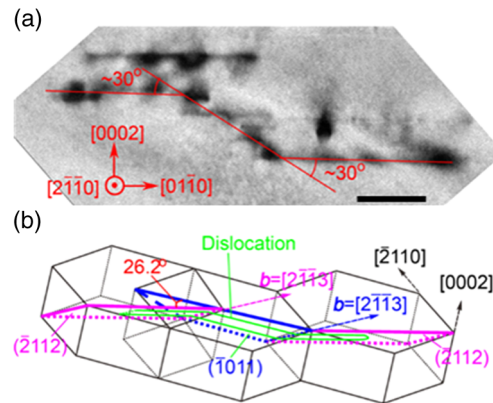

FIG. 4. Double cross slip of $\langle c + a \rangle$ dislocations. (a) Step-shaped $\langle c + a \rangle$ dislocation segment under $g = [0002]$ two-beam conditions around the $[2\bar{1}\,\bar{1}0]$ zone axis. The scale bar is 40 nm. (b) Schematic illustration of double cross slip.

fact that the angle between the inclined segment and the $[01\bar{1}0]$ segment is close to the angle between the $\{2\bar{1}\,\bar{1}\,2\}$ slip plane and the $\{10\bar{1}1\}$ slip plane ($\sim26°$), the dislocation may have cross slipped from a second-order primary plane (i.e., $\{2\bar{1}\,\bar{1}\,2\}$ plane) to a first-order primary plane (i.e., $\{10\bar{1}1\}$ plane), and then may have double cross slipped to the second-order primary plane again. The schematic illustration of the double cross-slip process is shown in Fig. 4).

As shown in a previous study [22], the hcp high-entropy phase plays a key role on the later stages of deformation in the bulk dual-phase HEA. A strength of ~800 MPa was realized at a strain of 65% in a dual-phase HEA containing ~84 vol% hcp and 16 vol. % fcc phase [22], respectively. In the present TEM study, we revealed the fundamental mechanisms of the deformation in the hcp high-entropy phase, especially the different types of active dislocation slips, both by *in situ* and postmortem observations. In hcp structured materials, the $\langle a \rangle$ and $\langle c+a \rangle$ dislocations are glissile while the $\langle c \rangle$ dislocations are sessile [27,28]. The $\langle a \rangle$ dislocations tend to solely slip on basal or prismatic planes, hence providing no shear contribution reaching out of the basal plane. The critical resolved shear stress (CRSS) of $\langle a \rangle$ dislocations is significantly lower than that of $\langle c+a \rangle$ dislocations in most conventional hcp metals [29,30]. According to the Taylor–von Mises criterion, at least five independent slip systems are necessary to achieve uniform and compatible deformation in polycrystalline material [29]. Slip only via $\langle a \rangle$ dislocations can thus not satisfy this criterion. Slip of $\langle c+a \rangle$ dislocations can provide additional independent slip systems to meet the Taylor–von Mises criterion and hence improve ductility. In the hcp high-entropy phase studied here, the nonbasal slip was observed through *in situ* TEM and $\langle c+a \rangle$ dislocations were frequently observed together with $\langle c \rangle$ and $\langle a \rangle$ dislocations, in line fractions 31% $\langle c+a \rangle$, 16% $\langle c \rangle$, and 53% $\langle a \rangle$, respectively. This high population of about 50% nonbasal dislocations proves that this phase can deform in a fully compatible fashion. Double cross slip of $\langle c+a \rangle$ dislocations was also found (Fig. 4 and Fig. S8). Cross slip spreads slip activity spatially on multiple nonparallel planes and hence promotes dislocation homogenization, annihilation, and multiplication processes [31,32]. These processes effectively improve uniform deformation, avoid strain localization, and thus contribute to high macroscopic ductility. The screw components of mixed $\langle c+a \rangle$ dislocations can move and also run out quickly through cross slip. Also, each double cross-slip event acts as a potential dislocation source [33–36]. This means that the activation of nonbasal slip systems not only helps in achieving kinematically compatible deformation but it is also the most efficient way of producing dislocation sources, thereby enabling massive dislocation multiplication. This acts twofold, through permanently replenishing dislocation flux and through increasing dislocation interactions.

Both features strongly contribute to strength and strain hardening.

Conventional hcp alloys show significant difference in CRSS between the $\langle a \rangle$ and $\langle c+a \rangle$ slip systems at ambient temperature, often exceeding a factor of 10, e.g., in Mg alloys [29,30]. Therefore, $\langle c+a \rangle$ slip is hard to activate in many hcp alloys. The c/a ratio is a key structure parameter of hcp alloys and directly linked to the lattice spacing [3,37]. The ideal value of the c/a ratio is 1.633, corresponding to a close packing of hard spheres. Compared to the ideal hcp structure, the lattice spacing of the basal plane increases for hcp metals with $c/a > 1.633$ and drops for $c/a < 1.633$ [37]. The resulting changes in packing density of the atoms in the different planes translates to a corresponding atomic plane roughness. This links the c/a ratio to the shear resistance that dislocations must overcome for gliding in terms of the Peierls model. Consequently, the predominant slip plane is basal $\langle a \rangle$ slip for hcp metals with $c/a > 1.633$ (e.g., Cd and Zn), but prismatic $\langle a \rangle$ slip for hcp metals with $c/a < 1.633$ (e.g., Ti and Zr). It is worth noting that a deviation from this trend can occur for Mg and Co; i.e., their prevalent slip system is basal $\langle a \rangle$ slip even though their $c/a < 1.633$. This anomaly is caused by a slight deviation of the c/a ratio from the ideal value and the zigzag nature of the atomic packaging in the prismatic and pyramidal planes [37]. Yet, in general, the c/a ratio is closely related to the structural plane features that govern activation of slip systems in hcp metals. Adjusting the c/a ratio by compositional tuning is therefore a most efficient way of lowering the atomic packing density of nonbasal planes, thus reducing the CRSS of nonbasal $\langle c+a \rangle$ dislocations [3,37]. In most established hcp alloys the approach of compositional tuning the c/a ratio is impeded by their rather limited solid solution range [6,7]. In contrast, the high-entropy concept is based on identifying such phases which tolerate massive solid solution, rendering them inherently immune to this critical limitation. The lattice parameters of the two phases in the $Fe_{50}Mn_{30}Cr_{10}Co_{10}$ (at. %) HEA were determined by x-ray diffraction (See Fig. S9 and Table VI in the Supplemental Material [4]). The lattice parameter of the fcc phase was determined to be $a_{fcc} = 3.608 \pm 0.002$ Å and those of the hcp phase $a_{hcp} = 2.544 \pm 0.002$ and $c_{hcp} = 4.110 \pm 0.001$ Å. This result reveals a significantly reduced c/a ratio of only 1.616 ± 0.001 compared to the ideal one of 1.633. This change originates from a compositional tuning rationale in which the massive alloying affects the two lattice parameters differently. It is thus also the reduction of the c/a ratio which enhances $\langle c+a \rangle$ slip in the current hcp high-entropy phase. Figure 5 shows some results regarding the change of the c/a ratios of Mg and Ti alloys as a function of their alloying content together with the observed deformation modes (detailed information is shown in Table SI in the Supplemental Material [4]) [3,6–13]. The deformation of pure Mg and Ti are both
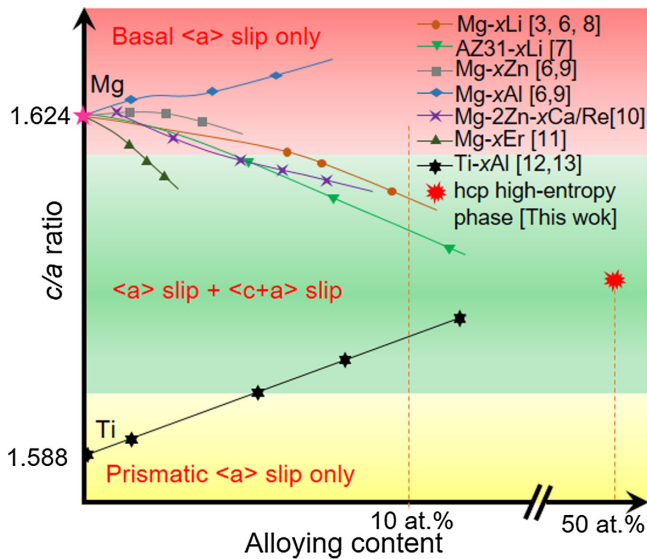
FIG. 5.   Overview of the c/a ratios of several Mg and Ti based hcp alloys with varying alloying content compared to the hcp high-entropy phase studied here. Three distinct regimes are indicated according to the activated crystallographic deformation modes [3,6–13].

dominated by pure $\langle a \rangle$ slip, explaining their limited formability [32,38,39]. Figure 5 shows that through adequate alloying, the c/a ratios of these two types of alloys can be adjusted to a certain extent, shifting them into a regime favoring activation of multiple deformation modes ($\langle a \rangle$ slip and $\langle c+a \rangle$ slip). Additional factors influencing glide system selection in these materials are the crystallographic orientation, grain size, deformation mode and stacking fault energy [39–45]. The hcp high-entropy phase studied here contains a large total alloy content of 50 at. % when taking Fe as the base element, thus significantly altering its c/a ratio. Our results show that this shift in the c/a ratio indeed leads to the activation of nonbasal $\langle c+a \rangle$ slip and frequent cross slip (Figs. 1–4), placing the hcp high-entropy phase into a range where multiple deformation systems become active, as shown in Fig. 5.

Our work reveals a novel pathway for the design of strong and ductile hcp structured alloys. It is based on the utilization of the high-entropy alloy concept and its effect on lattice parameter tuning with the aim to shift the c/a ratio into regimes where $\langle c+a \rangle$ dislocation slip is promoted in addition to $\langle a \rangle$ slip. Conventional hcp alloys have limited solid solution ranges, thus offering insufficient compositional tuning capabilities for changing the c/a ratio. The high-entropy concept with its massive solid solution characteristics allows us to explore new hcp structures which tolerate higher compositional variations, rendering them inherently immune to the critical solubility limits typical of conventional hcp materials. This approach thus opens a possible pathway for mitigating the intrinsic brittleness of conventional hcp materials.

*These two authors contributed equally to this work.
†liujiabin@zju.edu.cn
‡htw@zju.edu.cn
§d.raabe@mpie.de

[1] M. H. Yoo, S. R. Agnew, J. R. Morris, and K. M. Ho, Mater. Sci. Eng. A **319–321**, 87 (2001).
[2] M. H. Yoo. Metall. Trans. A **12**, 409 (1981).
[3] F. E. Hauser, P. R. Landon, and J. E. Dorn, Fracture of magnesium alloys at low temperature. Minerals Research Laboratory, Institute of Engineering Research, University of California, Berkeley.
[4] See Supplemental Material at http://link.aps.org/supplemental/10.1103/PhysRevLett.122.075502 for the comparison of c/a ratios and deformation modes of hcp alloys, the additional TEM results of dislocation types and cross slip, and the lattice parameters of $Fe_{50}Mn_{30}Co_{10}Cr_{10}$, which includes Refs. [3,5–13].
[5] Z. Li, K. G. Pradeep, Y. Deng, D. Raabe, and C. C. Tasan, Nature (London) **534**, 227 (2016).
[6] J. S. Park and Y. W. Chang, Adv. Mater. Res. **26–28**, 95 (2007).
[7] R. Li, F. Pan, B. Jiang, H. Dong, and Q. Yang, Mater. Sci. Eng. A **562**, 33 (2013).
[8] S. R. Agnew, J. A. Horton, and M. H. Yoo, Metall. Mater. Trans. A **33**, 851 (2002).
[9] H. L. Kim, J. S. Park, and Y. W. Chang, Mater. Sci. Eng. A **540**, 198 (2012).
[10] H. Ding, X. Shi, Y. Wang, G. Cheng, and S. Kamado, Mater. Sci. Eng. A **645**, 196 (2015).
[11] B. L. Wu, G. Wan, X. H. Du, Y. D. Zhang, F. Wagner, and C. Esling, Mater. Sci. Eng. A **573**, 205 (2013).
[12] H. R. Ogden, D. J. Maykuth, W. L. Finlay, and R. I. Jaffee, JOM **3**, 1150 (1951).
[13] J. C. Williams, R. G. Baggerly, and N. E. Metall, Mater. Trans. A **33**, 837 (2002).
[14] Y. Zhang, T. T. Zuo, Z. Tang, M. C. Gao, K. A. Dahmen, P. K. Liaw, and Z. P. Lu, Prog. Mater. Sci. **61**, 1 (2014).
[15] M. Feuerbacher, M. Heidelmann, and C. Thomas, Mater. Res. Lett. **3**, 1 (2015).
[16] R. Soler, A. Evirgen, M. Yao, C. Kirchlechner, F. Stein, M. Feuerbacher, D. Raabe, and G. Dehm, Acta Mater. **156**, 86 (2018).
[17] Y. J. Zhao, J. W. Qiao, S. G. Ma, M. C. Gao, H. J. Yang, M. W. Chen, and Y. Zhang, Mater. Des. **96**, 10 (2016).
[18] A. Takeuchi, K. Amiya, T. Wada, K. Yubuta, and W. Zhang, JOM **66**, 1984 (2014).
[19] F. Zhang et al., Nat. Commun. **8**, 15687 (2017).

[20] C. L. Tracy, S. Park, D. R. Rittman, S. J. Zinkle, H. Bei, M. Lang, R. C. Ewing, and W. L. Mao, Nat. Commun. **8,** 15634 (2017).

[21] Z. Li, F. Krmann, B. Grabowski, J. Neugebauer, and D. Raabe, Acta Mater. **136,** 262 (2017).

[22] Z. Li, C. C. Tasan, K. G. Pradeep, and D. Raabe, Acta Mater. **131,** 323 (2017).

[23] See Supplemental Material at http://link.aps.org/supplemental/10.1103/PhysRevLett.122.075502 for a movie of the detailed *in situ* process of the nonbasal slip.

[24] W. W. Hu, Z. Q. Yang, and H. Q. Ye, Acta Mater. **124,** 372 (2017).

[25] J. Geng, M. F. Chisholm, R. K. Mishra, and K. S. Kumar, Philos. Mag. **95,** 3910 (2015).

[26] J. Jain, P. Cizek, and K. Hariharan, Scr. Mater. **130,** 133 (2017).

[27] I. P. Jones and W. B. Hutchinson, Acta Metall. **29,** 951 (1981).

[28] Z. Wu and W. A. Curtin, Scr. Mater. **116,** 104 (2016).

[29] M. H. Yoo, Metall. Trans. A **12,** 409 (1981).

[30] K. Mathis, K. Nyilas, A. Axt, I. Dragomir-Cernatescu, T. Ungar, and P. Lukac, Acta Mater. **52,** 2889 (2004).

[31] Z. Wu and W. A. Curtin, Proc. Natl. Acad. Sci. U.S.A. **113,** 11137 (2016).

[32] Z. X. Wu, R. Ahmad, B. L. Yin, S. Sandlöbes, and W. A. Curtin, Science **359,** 447 (2018).

[33] B. Barkia, J. P. Couzinie, S. Lartigue-Korinek, I. Guillot, and V. Doquet, Mater. Sci. Eng. A **703,** 331 (2017).

[34] U. Messerschmidt and M. Bartsch, Mater. Chem. Phys. **81,** 518 (2003).

[35] J. S. Koehler, Phys. Rev. **86,** 52 (1952).

[36] F. Louchet and L. P. Kubin, Phys. Status Solidi A **56,** 169 (1979).

[37] J. P. Hirth and J. Lothe, *Theory of Dislocations* (Springer-Verlag, New York, 1982), p. 280.

[38] Z. Wu and W. A. Curtin, Nature (London) **526,** 62 (2015).

[39] P. Castany, F. Pettinari-Sturmel, J. Crestou, J. Douin, and A. Coujou, Acta Mater. **55,** 6284 (2007).

[40] S. Zaefferer, Mater. Sci. Eng. A **344,** 20 (2003).

[41] S. Sandlöbes, M. Friák, S. Korte-Kerzel, Z. Pei, J. Neugebauer, and D. Raabe, Sci. Rep. **7,** 10458 (2017).

[42] S. Sandlöbes, M. Friák, S. Zaefferer, A. Dick, S. Yi, D. Letzig, Z. Pei, L. F. Zhu, J. Neugebauer, and D. Raabe, Acta Mater. **60,** 3011 (2012).

[43] J. Gong and A. J. Wilkinson, Acta Mater. **57,** 5693 (2009).

[44] S. Sandlöbes, M. Friák, J. Neugebauer, and D. Raabe, Mater. Sci. Eng. A **576,** 61 (2013).

[45] S. Sandlöbes, Z. R. Pei, M. Friák, L. F. Zhu, F. C. Wang, S. Zaefferer, D. Raabe, and J. Neugebauer, Acta Mater. **70,** 92 (2014).